



Soft Matter

**Measuring Colloid-Surface Interaction Forces in Parallel
Using Fluorescence Centrifuge Force Microscopy**

Journal:	<i>Soft Matter</i>
Manuscript ID	SM-ART-03-2021-000461.R1
Article Type:	Paper
Date Submitted by the Author:	20-May-2021
Complete List of Authors:	LeFevre, Thomas; Montana State University Bozeman, Chemical & Biological Engineering Bikos, Dimitri; Montana State University Bozeman, Chang, Connie; Montana State University Bozeman, Chemical and Biological Engineering Wilking, James; Montana State University Bozeman, Chemical & Biological Engineering

SCHOLARONE™
Manuscripts

Measuring Colloid-Surface Interaction Forces in Parallel Using Fluorescence Centrifuge Force Microscopy

Thomas B. LeFevre^{1,2}, Dimitri A. Bikos^{1,2}, Connie B. Chang^{1,2}, and James N. Wilking^{1,2*}

¹Department of Chemical and Biological Engineering,

²Center for Biofilm Engineering,

Montana State University, Bozeman, MT, USA

Abstract

Interactions between colloidal-scale structures govern the physical properties of soft and biological materials, and knowledge of the forces associated with these interactions is critical for understanding and controlling these materials. A common approach to quantify colloidal interactions is to measure the interaction forces between colloids and a fixed surface. The centrifuge force microscope (CFM), a miniaturized microscope inside a centrifuge, is capable of performing hundreds of force measurements in parallel over a wide force range (10^{-2} to 10^4 pN), but CFM instruments are not widely used to measure colloid-surface interaction forces. In addition, current CFM instruments rely on brightfield illumination and are not capable of fluorescence microscopy. Here we present a fluorescence CFM (F-CFM) that combines both fluorescence and brightfield microscopy and demonstrate its use for measuring microscale colloidal-surface interaction forces. The F-CFM operates at speeds up to 5000 RPM, 2.5× faster than those previously reported, yielding a 6.25× greater maximum force than previous instruments. A battery-powered GoPro video camera enables real-time viewing of the microscopy video on a mobile device, and frequency analysis of the audio signal correlates centrifuge rotational speed with the video signal. To demonstrate the capability of the F-CFM, we measure the force required to detach hundreds of electrostatically-stabilized colloidal microspheres attached to a charged glass surface as a function of ionic strength and compare the resulting force distributions with an approximated DLVO theory. The F-CFM will enable microscale force measurements to be correlated with fluorescence imaging in soft and biological systems.

* Corresponding author: jwilking@gmail.com

42 I. INTRODUCTION

43

44 Soft materials are widespread in nature and industry.¹⁻⁸ Examples include food,^{9, 10} personal care
45 products,¹¹ biomedical supplies,¹² and biological tissues.¹³ These materials are characterized by
46 colloidal-scale structures such as drops,¹⁴ particles,¹⁵⁻¹⁷ and polymers,^{4, 18, 19} which range in size
47 from nanometers to micrometers, and the behavior of these structures govern material
48 properties.^{2, 3, 20, 21} A defining attribute of soft materials is their mechanical properties, and
49 knowledge of these properties is valuable for both fundamental and applied research. For
50 example, products like toothpaste must be formulated to achieve desired flow properties and
51 the mechanics of tissues and bio-gels play critical roles in diseases like cancer^{22, 23} and
52 osteoarthritis.^{24, 25} These properties are governed by interactions between colloidal
53 constituents;^{21, 26, 27} thus, characterizing colloidal interaction forces is important for
54 understanding and controlling soft material mechanical properties.^{28, 29}

55

56 A variety of tools exist for directly measuring colloidal interaction forces, which are both small
57 and wide-ranging, from 10^{-2} to 10^4 pN.³⁰⁻³² With optical trapping, colloids are brought close to
58 one another and the magnitude of the attractive or repulsive forces between them measured as
59 a function of separation distance.³³⁻³⁵ Tools like atomic force microscopy (AFM)^{36, 37} measure
60 interactions between colloids and a fixed surface. Both optical trapping and AFM provide high-
61 resolution force information, but measurements are typically performed one at a time, and are
62 not ideal for quantifying heterogeneous systems, which require many measurements to
63 construct statistically significant force distributions. Instead, techniques like magnetic tweezers^{32,}
64 ³⁸ and centrifugal force microscopy (CFM),³⁹⁻⁴⁴ which can perform multiple force measurements
65 in parallel are better suited for characterizing heterogeneous systems. CFM is a particularly
66 attractive technique because it is capable of multiple simultaneous measurements (i.e. force
67 multiplexing) and does not require significant device calibration or user training. A CFM
68 instrument is composed of a miniaturized microscope housed inside a swinging bucket
69 centrifuge. As the centrifuge spins, colloids suspended in liquid and interacting with a coverslip
70 are subjected to an effective gravitational force drawing them away from the surface. By
71 controlling the rotational speed of the centrifuge, well-defined forces can be applied to 100s of
72 individual colloids simultaneously; however, current CFM instruments rely on brightfield optical
73 microscopy to identify and track colloidal objects.³⁹⁻⁴⁴ This illumination technique is adequate for
74 measuring colloidal interaction forces but is limited with regard to spatial resolution and sample
75 characterization. Fluorescence microscopy offers enhanced spatial resolution and access to a
76 widevariety of sample labelling techniques, but the incorporation of fluorescence imaging into a
77 CFM has not yet been reported. Such an instrument would provide significant benefits for
78 characterizing complex soft and biological materials.

79

80 Here we present a fluorescence CFM (F-CFM) capable of performing both fluorescence and
81 brightfield microscopy in combination with microscale force measurements. The F-CFM can
82 perform 100s of interaction force measurements simultaneously. The F-CFM operates at speeds
83 up to 5000 RPM, 2.5× faster than those previously reported, yielding a 6.25× greater maximum
84 force for any given colloid and a resulting force range of 10^{-2} to 10^5 pN. Additionally, use of a
85 battery-powered GoPro video camera enables real-time transfer of microscopy video to a mobile
86 device during operation, and frequency analysis of the audio signal provided by on-camera
87 microphones correlates centrifuge rotational speed with the video signal. Wireless streaming
88 video allows observation and control of experiments in real time, similar to previous CFM
89 iterations.^{43, 44} Audio verification of speed, also not reported in previous iterations, allows
90 determination of centrifuge speed profiles in standard unmodified benchtop centrifuges to be
91 controlled through an external computer user interface. We validate the accuracy of the
92 instrument by measuring, at various effective gravities, the time required for fluorescent colloidal
93 microspheres to sediment from one imaging plane to another. To demonstrate the capability of
94 the F-CFM for performing multiple measurements in parallel, we measure the forces required to
95 detach 100s of electrostatically-stabilized colloidal microspheres attached to a charged glass
96 surface as a function of ionic strength and compare the resulting force distributions to a modified
97 Derjaguin-Landau-Verwey-Overbeek (DLVO) theory. The F-CFM will enable microscale force
98 measurements to be correlated with fluorescence markers in soft and biological systems.

99

100 II. METHODS

101

102 A. Instrument

103

104 The F-CFM design is based on a brightfield CFM developed for single-molecule force
105 multiplexing.⁴¹ Optical hardware and supporting electronics are housed in a cylindrical 3D-
106 printed clamshell enclosure that splits into two pieces, bisected by a plane parallel to the long
107 axis (**Fig. 1A**). Supporting electronics include a white brightfield light-emitting diode (LED) (**Fig.**
108 **1A, i and ii**), a blue fluorescent excitation LED (**Fig. 1A, iii and iv**), and a lithium polymer (LiPo)
109 battery (**Fig. 1A, v**). For brightfield illumination, a diffuse white LED is soldered to a customized
110 circuit board (PCB) along with a 10-k Ω resistor and Japanese solderless terminal (JST) male
111 connector socket (**Fig. 1A, right inset**). For fluorescent illumination, a blue LED is soldered to
112 another customized PCB along with a 10- Ω resistor and JST male connector socket (**Fig. 1A, left**
113 **inset**). The battery can be connected to the brightfield LED, the blue fluorescent LED, or both –
114 resulting in three available illumination modes. When both LEDs are operational, two batteries
115 are used, and a piece of neutral density filter film (ND = 1.2) is placed over the brightfield LED to
116 reduce the reflection of the fluorescence optical beam off the brightfield LED. The F-CFM is
117 operated in any of these modes by connecting the appropriate LiPo battery to the desired LED

118 during instrument assembly. The camera and optical hardware fit into a custom-designed recess
119 within the clamshell housing (**Fig. 1B**). After the F-CFM module is assembled and battery wiring
120 harness connected, the second clamshell piece closes around the module (**Fig. 1C**) and the entire
121 module with housing is inserted into the bucket of a commercially available centrifuge
122 (ThermoFisher Sorvall Legend X1R).

123
124 During operation, the centrifuge swinging buckets do not fully extend 90° to the rotational axis z
125 during operation, resulting in a non-normal force vector acting on the sample cell. This is
126 illustrated in **Fig. 1D**. The force vector is 76.6° from perpendicular at 300 RPM and 80.7° from
127 perpendicular at 1000 to 5000 RPM (see **SI Note 1** and **SI Fig. 1**) The objective tube, containing
128 the sample cell module and objective, connects to a 3D-printed fluorescence cube, containing a
129 495-nm dichroic mirror and 520-nm bandpass emission filter, which connects to the focusing lens
130 tube to form a tubular microscope which is attached to a camera (**Fig. 1E**). The 472-nm bandpass
131 excitation filter fits inside the blue LED housing. The sample cell, constructed from two circular
132 glass coverslips separated by a spacer to create a sealed shallow sample well, is contained in a
133 two-part 3D-printed housing constructed from a sample cell holder and lid that screws into the
134 objective microscope tube (**Fig. 1E, inset**). Mounting the sample cell on the interior of the
135 objective tube rather than the exterior end of the tube reduces deformation of the sample cell
136 during centrifugation because the thick walls of the objective tube resist deformation better than
137 the thin threads connecting an exterior sample cell holder to the objective tube. This provides
138 less change in focus throughout the experiment, even at 5000 RPM, the highest RPM for which
139 our buckets are rated. A complete exploded-view diagram and parts ordering information are
140 listed in **SI Fig. 2**. CAD files in STEP format for all 3D-printed components are included as
141 supplemental files as well.

142
143 Recent advances in camera technology enable the F-CFM. Here, we use a compact, wireless
144 GoPro Hero 5 action camera. The compact form factor of the camera allows more room for
145 fluorescence optical components than previous CFM designs.³⁹⁻⁴¹ The wireless feature allows the
146 video to be viewed in real time through an application on a smartphone, which also allows the
147 user to start and stop recording remotely. The live video feed is clear up to 4000 RPM and exhibits
148 only minor interference up to 5000 RPM. The GoPro camera has a $6.17 \text{ mm} \times 4.55 \text{ mm}$ CMOS 12-
149 megapixel sensor capable of 4K video at 30 frames per second (fps) and 1080p video at 120 fps,
150 stores video on an SD card and requires no electronics knowledge to operate. Here, we use a
151 shorter optical path ($\approx 40 \text{ mm}$) than previous designs ($\approx 90 \text{ mm}$), which require turning mirrors.<sup>39-
152 41</sup> This configuration leads to aberrative vignetting and optical distortion in the corners of the
153 image but offers an acceptable compromise by providing room for important optical
154 components.

155

156 B. Fabrication

157
158 Construction of F-CFM components is straight-forward and does not require extensive
159 fabrication, programming, or electronics knowledge. The M12 threaded connector that attaches
160 the camera to the focusing tube is made by threading a plain aluminum tube (12 mm O.D. × 10
161 mm I.D.) using an M12 die along with a die wrench, pipe cutter, and vise. The brightfield LED is
162 soldered to a simple customized PCB (oshpark.com) along with a JST connector and 10-kΩ
163 resistor. The fluorescence LED is soldered to a different customized PCB along with a JST
164 connector and 10-Ω resistor. The brightfield LED requires a strong resistor to prevent
165 oversaturation of the brightfield images, and the fluorescence LED requires a weak resistor to
166 generate enough light to excite the fluorescent dye in the sample. All other components are
167 purchased from optics companies or 3D-printed with a Stanley Model 1 fused deposition
168 modeling (FDM) printer with poly-lactic acid (PLA) 1.75-mm diameter filament. See **SI Note 2** for
169 assembly information.

170

171 C. Experimental Protocol

172

173 Circular glass coverslips (Thomas Scientific, diameter 18 mm, No. 2 thickness) are cleaned by
174 sonicating for 15 min in each of the following: acetone, isopropanol, 2.0 M NaOH, and pure
175 distilled water, in that order. Prior to the final distilled water sonication step, the coverslips are
176 rinsed several times in pure distilled water to remove excess NaOH. After the final sonication
177 step, the slides are dried with nitrogen. Donut-shaped annular spacers (I.D. = 7 mm, O.D. = 15
178 mm) are cut from 102.5 μm ± 3.6 μm thickness Kapton tape using a craft cutter (Silhouette
179 CAMEO 2) and adhered to one slide (see **SI Note 3** and **SI Fig. 3**). An annular bead of UV-curing
180 optical adhesive (Norland 61) is deposited inside the annular tape ring on the slide. This bead of
181 adhesive protects the central region of interest on the slide from being disturbed by air bubbles
182 that form on the edge of the tape during centrifugation, likely due to compression of the tape.
183 After curing the bead of UV adhesive under UV light until hardened (20 – 300 s depending on the
184 light source), 25 μL of the colloid suspension is pipetted into the shallow well created by the
185 annular spacer and slide. Another cleaned slide is then placed on top of the tape spacer, sealing
186 the sample inside. The inadvertent incorporation of air bubbles must be avoided as their
187 movement during measurements leads to undesired liquid flows.

188

189 Once the sample cell is prepared, it is loaded into the sample cell holder which screws into the
190 objective tube. The distance from the sample cell to the objective is adjusted by screwing in the
191 sample cell holder until the interior surface of interest is in focus. This is accomplished by looking
192 at the built-in camera display screen or by attaching the camera to a monitor with the camera

193 mini-USB connection. The sample cell must be illuminated manually, independent of the housing
194 during the focusing adjustment before the F-CFM is placed inside the clamshell holder.

195
196 After focus is achieved, the F-CFM module is enclosed in the clamshell housing and loaded into a
197 centrifuge bucket. The two sides of the housing are held together by the snug fit within the
198 centrifuge bucket. The weight of the counterbalance at the opposing bucket is verified using an
199 electronic scale, the lid is closed, and the centrifuge is started. When the run is complete, the
200 centrifuge is allowed to come to rest and opened, the camera recording is stopped, and the video
201 files are downloaded to a computer. The onset of centrifuge rotation is distinctly audible in the
202 recorded video, providing a reference point for video image data to be synced with speed data.

203
204 The centrifuge used in this study is a swinging bucket ThermoFisher Sorvall Legend X1R with 400-
205 mL buckets (TX-400, p/n 75003655), custom-ordered for PC-control. Operation is controlled by
206 PC instead of the front control pad and records the RPM profile by reporting speed values every
207 0.5 s. The RPM is measured using a built-in Hall effect sensor and magnets in the rotor base.
208 Detailed speed profiles can be programmed from the included PC control software. A centrifuge
209 without PC control could also be used by manually increasing the centrifuge speed in a stepwise
210 fashion using the centrifuge control pad.

211
212 Video files (.mp4) are downloaded from the GoPro SD card onto a PC. Using the FFmpeg toolbox
213 in MATLAB, the .mp4 files are converted into .tiff stacks. Here, for ease of analysis, only one out
214 of every hundred frames is kept for analysis. The frame is cropped from its original 1280×720 px
215 to a central 320×300 px rectangle in the region of best focus (**Fig. 2**). These frames are then
216 corrected for drift in Imaris 9.2.1 software. The resulting drift-corrected frames are analyzed one-
217 by-one manually by counting the number of colloids in each frame and recording the colloid
218 counts in a spreadsheet. The frame numbers are synchronized with the reported centrifuge
219 speed to determine the RPM and effective gravity g_{eff} associated with each colloid count. The
220 centrifugal force acting on each microsphere is defined by $F_c = m\omega^2 r$ where r is the moment
221 arm of the centrifuge (0.15 m), ω is the rotational velocity, and m is the effective mass of the
222 colloid. Here, $m = V_c(\rho_c - \rho_f)$, where V_c is the volume of the colloid, ρ_c is the density of the
223 colloid and ρ_f is the density of the fluid.

224
225 Independent verification of the reported centrifuge speeds is performed by audio analysis of the
226 .mp4 video files. Using a custom MATLAB R2019b routine, we extract the 48000 Hz stereo
227 samples recorded by the left channel of the audio track. The GoPro provides two channels of
228 audio (right and left) which capture similar audio information. Here, we have chosen the left
229 channel for analysis. To match the centrifuge reporting frequency of 0.5 s^{-1} , we fit audio signal
230 clips of 0.5 s duration using a sum-of-sines routine found within the MATLAB Curve Fitting

231 Toolbox. Thus, we can associate each video frame, taken at 25 fps in PAL format, to a
232 corresponding audio clip containing 2000 samples. After fitting the resulting audio waveform
233 using the sum-of-sines fitting routine, frequency information is extracted from the fit parameters,
234 associating an RPM with each 0.5 s time interval. It is convenient to record in PAL format rather
235 than NTSC format to ensure an integer number of video frames per second; this option is
236 available in the “Preferences” menu of the GoPro.

237

238 D. Safety Considerations

239

240 Care must be taken to properly balance the centrifuge. To accomplish this, we set opposing
241 bucket weights to within 1 g of each other. Larger mass imbalances will lead to centrifuge
242 vibration during operation. More importantly, the centers of mass of opposing buckets must
243 match closely as small differences will lead to centrifuge vibration. Given the low cost of a F-CFM
244 module and housing (see **SI Fig. 2**), we counterbalance the F-CFM with a second, identical
245 complete F-CFM module and housing in the opposing bucket. We find this approach is simpler
246 than attempting to replicate the F-CFM module mass distribution with an assembly of similarly
247 weighted objects, and it provides the option of running two different experiments
248 simultaneously.

249

250 Care must also be taken to avoid LiPo battery leakage and fire. LiPo batteries should be inspected
251 for damage after each run. If the batteries become dented or smashed, they should be stored in
252 a fireproof LiPo battery bag (e.g. Suncentech 180 × 230 mm LiPo Guard battery storage bags) and
253 brought to an electronics retailer for recycling. In initial testing, some of our large batteries (1000
254 mAh) did leak fluid after extended operation at high speeds; thus, we prefer to use small batteries
255 (40 - 400 mAh) to reduce the risk of rupture, leakage, and fire. These small batteries provide more
256 than enough current to operate the LED for hours, and we have not observed any damage or
257 leakage due to centrifugation. The centrifuge and buckets are capable of speeds up to 5000 RPM.
258 However, in most cases we prefer to limit our experiments to a maximum speed of 4700 RPM to
259 reduce stress on the camera, batteries, and LEDs.

260

261 The F-CFM is housed within a custom-built guarding enclosure composed of an extruded
262 aluminum frame (80/20 brand) and 1/4-in. polycarbonate (8020.net) (**SI Fig. 4**). Although our
263 centrifuge was custom-ordered, it contains standard safety features such as thick steel plates
264 surrounding the centrifugation chamber and an automatic override stop when excess vibration
265 is detected. Since our centrifuge buckets are well-balanced and still within the weight threshold
266 for which the buckets are rated, this polycarbonate guarding is simply meant to help contain
267 debris in the unlikely event of centrifuge failure.

268

269 III. RESULTS AND DISCUSSION

270

271 A. Image Quality

272

273 To assess the image quality provided by the F-CFM, we image a photomask printed with a grid of
274 uniform circular dots ($d = 10 \mu\text{m}$) (**Fig. 2A**). This video frame image measures 1280×720 px. The
275 image edges are out-of-focus because we use a short focal length focusing lens. The out-of-focus
276 area is likely due to comatic and spherical aberrations. To quantify the aberration, we measure
277 the aspect ratio (AR) of each dot using ImageJ and plot the aspect ratio as a function of radius R
278 from the center of focus (**Fig. 2B**). A perfect circle has an aspect ratio of 1, and the aspect ratio
279 increases as aberration increases. The peak of the curve, with an aspect ratio of 1.6, occurs ~ 575
280 px from the center of focus. The aspect ratio then dips slightly at the outer edges of the image
281 due to refraction of the light rays that reach the photomask at the highest angle. The center of
282 focus was determined by defining all the dots with $AR = 1$ and then finding the center of that
283 circle. The center of focus is near, but not directly aligned with the center of the image because
284 the objective, focusing lens, and camera sensor are not perfectly aligned. Fig. 2B provides a
285 measure of aberration across the image, and this information can be used to characterize a
286 region of acceptable image quality. For example, a circle (white dashed line) with $R = 300$ px
287 enclosing average hole aspect ratios $AR_{\text{hole}} \leq 1.25$ is shown in Fig. 2A. Different experiments will
288 require different ranges of acceptable image quality.

289

290 To demonstrate the capability of the F-CFM in differentiating two distinct but identically-sized
291 colloid populations using fluorescence, we image an aqueous suspension of microspheres
292 containing green and red fluorescent microspheres (Bangs Laboratories; green: $\bar{d} = 8.3 \pm 0.224$
293 μm (UMDG003) and red: $\bar{d} = 8.3 \pm 0.28 \mu\text{m}$ (UMFR003)). The microspheres are nearly identical in
294 size and thus indistinguishable with brightfield imaging alone (**Fig. 2C**). The red fluorescent
295 microspheres are not excited by the blue LED illumination, and thus are effectively non-
296 fluorescent under these imaging conditions; thus, the two microsphere populations are clearly
297 distinguishable when imaged by the F-CFM in fluorescence mode (**Fig. 2D, E**).

298

299 Fluorescence biophysical force measurements (e.g. single-molecule) comprise a potentially
300 important application for the F-CFM. Single-molecule force measurements require high-
301 precision, sub-pixel particle tracking within 10s of nm, which can be performed using the F-CFM.
302 To demonstrate, we adhere fluorescently-labelled, polystyrene colloids ($\bar{d} = 1.0 \mu\text{m}$, 1 wt%,
303 Thermo Scientific, G0100) to the inner surface of a water-filled sample cell, place the F-CFM
304 module on an optical table to reduce vibrations, and record individual beads for 10 s (**Fig. 2F**). A
305 radial symmetry particle tracking method records the center of each colloid as a function of time
306 with a maximum resolution of ± 0.027 px corresponding to ~ 2.7 nm. The x (**Fig. 2G**) and y (**Fig.**

307 **2H)** positions of a single representative bead fluctuates by ± 20 nm. This bead tracking resolution
308 is consistent with previous CFM devices. We chose a radial symmetry particle tracking method⁴⁵
309 over alternatives (e.g. centroid, Gaussian) for its accuracy, speed, and MATLAB graphical user
310 interface (see **SI Note 4**).

311

312 B. Force Range

313

314 The F-CFM can apply a broad range of forces to colloidal particles. The force range is set by r , ω ,
315 and m . Here, our r and minimum ω_{\min} are comparable to other commercial centrifuges; thus, the
316 minimum force that can be applied practically is comparable to that reported for other CFMs
317 ($F_{c,\min} \approx 10^{-2}$ pN). However, our $\omega_{\max} = 5000$ RPM is 2.5 \times greater than values reported for other
318 CFMs ($\omega_{\max} = 2000$ RPM). Since $F_c \propto \omega^2$, this provides a 6.25 \times increase in the maximum force,
319 compared to other CFMs.³⁹⁻⁴¹ For a polystyrene microsphere with $d = 1$ μm and $\rho_c = 1.06$ g/cm^3
320 suspended in water and run at 2000 RPM, the centrifugal force acting on the microsphere, $F_{c,\max}$
321 ≈ 0.2 pN, while at 5000 RPM, $F_{c,\max} \approx 1.3$ pN. The maximum force can be increased by increasing
322 d or ρ_c , which increases m . For example, from a practical perspective, the largest, most dense
323 colloid would likely be a silica microsphere with $d \approx 20$ μm and $\rho_c = 2.6$ g/cm^3 . At $\omega_{\max} = 5000$
324 RPM, this colloid would experience $F_{c,\max} \approx 10^5$ pN. Thus, here we report the force range of the F-
325 CFM to be 10^{-2} to 10^5 pN.

326

327 C. Force Validation

328

329 Most experiments with the F-CFM will subject colloidal suspensions to a well-defined centrifugal
330 force field. While this force is straightforward to calculate from known parameters and should
331 not require calibration, here we offer a simple sedimentation experiment to validate our force
332 predictions. We measure the time required for monodisperse, fluorescently-labelled,
333 polystyrene colloidal microspheres ($\bar{d} = 4.19 \pm 0.27$ μm , 0.97 wt %, $\rho_c = 1.06$ g/cm^3 , Bangs
334 Laboratories, FSDG006) to sediment from the top of the sample cell to the bottom at different
335 rotational velocities, convert these times to sedimentation velocities, and compare the
336 experimentally-measured velocities to theoretical predictions.

337

338 With the F-CFM module focused on the colloids at the bottom inside of the sample cell, the F-
339 CFM module is turned upside down to let the microspheres sediment to the inner surface of the
340 coverslip nearest the camera (i.e. "top") (**Fig. 3A**). The total time required for the microspheres
341 to sediment the thickness of the sample cell under gravity g is about 2 min, so the F-CFM module
342 is allowed to sit upside down for 5 min to ensure the microspheres have reached the top of the
343 sample cell before the measurement is started. Then we centrifuge the sample in the F-CFM and
344 measure the time required for the microspheres to sediment to the bottom of the sample cell.

345
 346 For each measurement, the centrifuge rotation is quickly ramped up to a fixed rotational speed
 347 and held at that speed until the colloids reach the inner surface of the coverslip farthest from the
 348 camera (i.e. “bottom”) (**Fig. 3B**). The centrifuge routine is systematically varied for a range of
 349 average rotational speeds, from 150-400 RPM, corresponding to accelerations ranging from 49-
 350 216 m/s² and a g_{eff} range of 5-22 g . Effective gravity, or relative centrifugal force (RCF), is
 351 calculated using $g_{\text{eff}} = 11.18r\left(\frac{Q}{1000}\right)^2$ where r is the moment arm of the centrifuge (here, $r = 15.0$
 352 cm) and Q is the RPM.

353
 354 The terminal velocity v_t is determined by dividing the settling distance by the measured
 355 sedimentation time. The settling distance is set by the thickness of the sample cell h_c which is set
 356 by the thickness of the Kapton tape ($102.5 \pm 3.6 \mu\text{m}$). Loading and initiating the centrifuge takes
 357 30 ± 5 s, during which time the colloids sediment $19.7 \pm 2.5 \mu\text{m}$; so, for our validation, the settling
 358 distance under g_{eff} is the modified thickness $h_m = 82.8 \pm 6.2 \mu\text{m}$. Even at the low colloid
 359 concentrations used here (< 1.0 wt %), many of the microspheres interact with one another
 360 hydrodynamically, settle together and arrive at the bottom of the sample cell sooner than those
 361 that sediment individually (**SI Video 1**). Thus, the sedimentation time is defined as the time from
 362 the start of the centrifuge rotation to the time at which all the individual microspheres have
 363 reached the bottom surface and are fully in focus. A plot of the measured v_t as a function of g_{eff}
 364 is shown in **Fig. 3C**.

365
 366 To compare these velocity results with expected values, we balance the force due to g_{eff} with the
 367 Stokes’ drag force on a sphere and solve for the terminal velocity of a sinking sphere: $v_t = \frac{2(\rho_c - \rho_f)}{9\eta} g_{\text{eff}} a^2$. Here, η is the dynamic viscosity of the medium, ρ_c is the density of the colloid, ρ_f is the
 368 density of the fluid medium, g_{eff} is the effective gravitational acceleration (RCF), and a is the
 369 radius of the colloid (see **SI Note 5** for more details). For each experiment, we calculate the
 370 average g_{eff} over the time frame provided by the observed settling time and plot the predicted v_t
 371 as a function of g_{eff} . The predicted v_t plotted as a function of g_{eff} agrees well with our
 372 measurements (**Fig. 3C**). The two gray dashed lines in Fig. 3C indicate the upper and lower
 373 predictions for v_t based on uncertainty in h_m , a , and sample temperature ($20 \text{ }^\circ\text{C} \leq T \leq 23 \text{ }^\circ\text{C}$), with
 374 the latter dictating the water viscosity ($0.9321 \text{ cP} \leq \eta \leq 1.0016 \text{ cP}$). The measurements fall almost
 375 entirely within the two bounds, confirming that we are accurately reporting g_{eff} acting on colloids
 376 in the F-CFM. The few points lying below the lower bound can be attributed to potential
 377 variations in tape thickness (i.e. sedimentation distance) and colloid density, and the fact that we
 378 wait for all colloids to reach the lower surface, thus effectively excluding the fastest settling
 379 colloids, which are likely interacting hydrodynamically, from our measurements.

381

382 D. Validation of Centrifuge Rotational Frequency with Audio Signal Analysis

383
384 Instantaneous rotational frequencies, reported as centrifuge speed RPMs, may be independently
385 validated by analysis of the audio signal recorded by the GoPro microphone during F-CFM
386 operation (**Fig. 4**). Audio sample waveforms are a record of the sounds produced by the physical
387 motion of the rotor, effectively providing a sinusoidal signal wherein rotational frequency
388 information is encoded. To illustrate this, we record an audiovisual movie of a linear ramp of
389 centrifuge speed from 0 to 5000 RPM during which audio is recorded at a sampling rate of 48
390 kHz. For the case of a F-CFM movie taken at 25 fps, each image frame represents a duration of
391 0.04 s. To compare the data obtained using audio signals with the data reported by the centrifuge
392 magnetic encoder, we divide the audio samples into 0.5-s intervals, each corresponding to 24
393 kHz samples (**Fig. 4A-C**, black lines). Using a customized MATLAB routine (see **Experimental**
394 **Protocol**), we fit these sample traces to a sinusoidal function, $I = A \sin(ft + \varphi)$ where I is the
395 recorded sample intensity (arbitrary units), A is the amplitude, f is the frequency in rad s^{-1} , t is
396 time, and φ is the offset (**Fig. 4A-C**, red lines) which tracks the waveforms. Every 0.5 s interval in
397 the movie is given a sine fit, and fitting parameter frequency f is used to determine the RPM value
398 (**Fig. 4D**). At centrifuge speeds < 1000 RPM, cumulative acoustic effects mask the waveform
399 frequency information, but for values > 1000 RPM, any harmonic effects are minimized, and
400 values track with those reported by the on-board magnetic encoder (**Fig. 4D**, inset). Individual
401 measurements in this range routinely differ by $< 3.0\%$ from the magnetically-encoded values.

402 403 E. Colloid Detachment Force Measurements

404
405 To demonstrate the capability of the F-CFM for performing multiple force measurements in
406 parallel, we induce attractive interactions between electrostatically-stabilized colloids with a
407 negative net surface charge and a negatively charged-glass coverslip and measure the forces
408 required to remove these colloids from the coverslip. We explore a range of attractive forces by
409 suspending monodisperse polystyrene/iron oxide microbeads (Sigma-Aldrich, 49664, 5.0 wt %, \bar{d}
410 $= 10.41 \pm 0.13 \mu\text{m}$, $\rho_c = 1.71 \text{ g/cm}^3$) in 0.25 \times (ionic strength $I = 0.053 \text{ M}$) phosphate buffered saline
411 (PBS) solution and varying the concentration of NaCl (0.1 M, 0.5 M, 1.25 M, and 2.5 M). The
412 interactions between a charged microsphere and like-charged wall are described by DLVO theory
413 as the sum of a van der Waals attraction and an electrostatic repulsion. The addition of salt to
414 the colloidal suspension screens the electrostatic repulsion, thus increasing the relative
415 contribution of the van der Waals attraction. PBS is added to buffer the pH to mitigate changes
416 in surface charge with changes in ionic strength.⁴⁶ For experiments with 0.25 \times PBS, the pH
417 decreases from 7.6 to 6.6 as the concentration of added NaCl increases from 0.1 M to 2.5 M.

418

419 For each measurement, the suspension is loaded into the sample cell, and the colloids settled
420 and adhered to the interior glass surface of the coverslip. The cell is then oriented such that the
421 g_{eff} acts to draw the colloids away from the surface, and the centrifuge rotational speed is ramped
422 up at 8.9 RPM/s from 0 - 4700 RPM, corresponding to 1 - 283 RCF. Colloids detach with increasing
423 rotational speed (**Fig. 5A**, **SI Video 2**, and **SI Video 3**). Colloid detachment between sequential
424 frames is determined using a manual image analysis process (**Fig. 5B** and **SI Note 6**). Detachment
425 counts are normalized to the initial number of attached colloids to determine the fraction of
426 colloids detached f_d , averaged across three runs per condition with 100-189 colloids tracked per
427 run, and plotted as a function of F_c (**Fig. 5C**). We observe that most colloids detach within the
428 range of applied forces. In addition, the force required to detach colloids increases with
429 increasing ionic strength. To better visualize the dependence of colloid attachment strength as a
430 function of ionic strength, we plot bead-detachment events for each of the four different
431 conditions as probability distributions (**Fig. 5F**). We find that the data are fit well by a log-normal
432 probability distribution (see **SI Table 3**), with the mode of the distribution increasing with
433 increasing ionic strength.

434
435 To calculate the expected strength of the colloidal interaction with the glass surface, we use a
436 modified DLVO model.⁴⁷ Colloidal interactions are commonly characterized by an interaction
437 potential where the interaction energy U is plotted as a function of the gap between the two
438 surfaces h ; here, instead, for comparison with our experimental force measurements, we
439 calculate and plot the total interaction force F_I as a function of h . For our system, the modified
440 DLVO model predicts two minima: a deep primary minimum at small separation distances ($h <$
441 0.5 nm) and a shallower secondary minimum at intermediate distances ($h \approx 2$ nm). A
442 representative $F_I(h)$ curve for one solution condition (0.5 M NaCl + 0.25× PBS) is shown in **Fig. 5D**
443 (see **SI Note 7** for DLVO equations and assumptions). During loading, as the microspheres are
444 drawn to the glass surface by gravity, they will be drawn into the secondary minimum; however,
445 they are unlikely to overcome the barrier to enter the primary minimum. Thus, we assume the
446 force F_d , required to remove the colloids from the surface of the glass at a separation distance h
447 is equal to the depth of the secondary minimum (**Fig. 5D**, dashed lines and inset).

448
449 To compare our results with expected values, we co-plot the force values associated with the
450 mode of each distribution from Fig. 5F as a function of ionic strength (**Fig. 5E**, solid blue circles)
451 together with predictions from the modified DLVO model (**Fig. 5E**, gray dashed lines). To
452 represent the uncertainty in surface charge potential⁴⁸ of the glass surface ψ_g and colloid surface
453 ψ_{cs} (see **SI Note 7**) we include two limiting cases as bounding lines: a high surface charge case (ψ_g
454 $= 300$ mV, $\psi_{cs} = 100$ mV) represented by the lower gray dashed line in Fig. 5E, and a low surface
455 charge case ($\psi_g = 150$ mV, $\psi_{cs} = 30$ mV) represented by the upper gray dashed line in Fig. 5E. We
456 find good agreement between experimental and expected detachment force values at low ionic

457 strength, but deviation at higher ionic strengths, with the calculated detachment force F_d higher
458 than the observed values. These differences could be attributed to surface charge uncertainty,⁴⁹⁻
459 ⁵⁶ spatial heterogeneities of the glass substrate surface potential,⁵⁷⁻⁶⁰ and surface roughness.^{31,}
460 ^{37, 61-65} Despite the disagreement at high ionic strength, our results reflect the capability of the F-
461 CFM to perform 10s to 100s of force measurements in parallel.

462
463 The F-CFM could be used to perform a variety of other parallel force measurements including
464 measurement of other colloidal interaction potentials (e. g. depletion and steric), single molecule
465 forces³⁹⁻⁴¹, microbial adhesion^{41, 66} and emulsion stability under compression in real time. Future
466 iterations of the F-CFM design could benefit from additional modifications. For example, a second
467 camera sensor could be added below the sample cell to allow transmitted light imaging
468 separately and concurrently with fluorescence imaging. This would improve the image quality for
469 both the transmitted and fluorescence image compared to the current combined “two-in-one”
470 fluorescence and brightfield image. A motorized sample holder that can move in the z-axis could
471 be incorporated for precise real-time mechanical image focusing. Currently, the sample is
472 focused manually at the start of the experiment and cannot be adjusted during the experiment.
473 The ability to move the sample in the z-axis while the centrifuge is spinning would allow focusing
474 on samples as they change position in the sample cell. Real-time focusing could also prevent the
475 reduction in clarity caused by flexing of the sample cell out of the focal plane inherent in high-
476 speed experiments. A second fluorescence cube could be integrated to allow for multiple
477 fluorophores to be imaged in a single run. This would require additional miniaturization of some
478 components or a larger swinging bucket. Mirrors could be added to directly image the bottom of
479 the surface of interest, allowing non-transparent substrates to be characterized. Other mirror
480 configurations could also allow the sample to be imaged from the side in order to track colloid
481 motion after detachment, although this would limit the number of in-focus colloids. Further
482 miniaturization and ruggedization would also allow the F-CFM to be incorporated into a fixed
483 rotor ultracentrifuge, enabling detachment force measurements on colloids such as bacteria and
484 viruses. Fluidic pumps could also be integrated into the empty remaining centrifuge buckets to
485 alter solution conditions during centrifugation, for example, enabling the concentration of
486 electrolytes in the suspension to be tuned until the point of colloid detachment. Biological
487 samples could be characterized by functionalizing the glass cover slips with treatments such as
488 silane followed by ligands of interests. Alternatively, a different transparent material such as
489 PMMA or polypropylene could be used in place of cover slips if the functionalization is better
490 suited to that material.

491

492 **IV. CONCLUSION**

493

494 To our knowledge, the F-CFM is the first CFM to incorporate fluorescence microscopy.
495 Additionally, the F-CFM is the first CFM used for colloid interaction force measurements and the
496 first CFM to operate up to 5000 RPM. This F-CFM is easy to assemble, requiring only basic
497 knowledge of electronics and fabrication. Additionally, the audio microphone provides highly
498 accurate rotational speed information for CFM configurations that lack a centrifuge with a
499 computer interface or on-board magnetic encoder. The wireless F-CFM provides high resolution
500 video with acceptable levels of aberrative vignetting to perform nm-scale, sub-pixel particle
501 tracking. Three illumination modes are available: brightfield, fluorescence, and combined
502 brightfield and fluorescence. Using the F-CFM, we induce attractive interactions between 100s
503 of colloids and a glass coverslip, measure their adhesion force as a function of ionic strength, and
504 show excellent correspondence with prediction at low ionic strength using a modified DLVO
505 model.

506

507 **Conflicts of interest**

508 There are no conflicts of interest to declare.

509

510 **Acknowledgements**

511

512 Special thanks to Wesley Wong and Darren Yang for generously showing us their CFM and
513 explaining its construction and operation. We also thank Matthew Griffin and Mandy Rutherford
514 from the Montana State University Makerspace for their help in the early design stages of this
515 project, and Aaron D. Benjamin for useful discussions.

516

517 **Funding**

518

519 This work was supported by the National Science Foundation (DMR-1455247, DMR-1753352, and
520 OIA-1736255).

521

522 **References Cited**

523

- 524 1. M. Daoud, S. N. Lyle and C. E. Williams, *Soft Matter Physics*, Springer Berlin Heidelberg, 2013.
- 525 2. P. M. Chaikin and T. C. Lubensky, *Principles of Condensed Matter Physics*, Cambridge University
526 Press, 2000.
- 527 3. W. B. Russel, W. B. Russel, D. A. Saville and W. R. Schowalter, *Colloidal Dispersions*, Cambridge
528 University Press, 1991.
- 529 4. M. Rubinstein and R. H. Colby, *Polymer Physics*, OUP Oxford, 2003.
- 530 5. T. Farjami and A. Madadlou, *Trends in Food Science & Technology*, 2019, **86**, 85-94.
- 531 6. T. Kokubo, H. M. Kim and M. Kawashita, *Biomaterials*, 2003, **24**, 2161-2175.
- 532 7. M. C. Marchetti, J. F. Joanny, S. Ramaswamy, T. B. Liverpool, J. Prost, M. Rao and R. A. Simha,
533 *Rev. Mod. Phys.*, 2013, **85**, 47.

- 534 8. M. M. Fryd and T. G. Mason, in *Annual Review of Physical Chemistry, Vol 63*, eds. M. A. Johnson
535 and T. J. Martinez, Annual Reviews, Palo Alto, 2012, vol. 63, pp. 493-518.
- 536 9. R. Mezzenga, P. Schurtenberger, A. Burbidge and M. Michel, *Nature Materials*, 2005, **4**, 729-740.
- 537 10. A. Donald, *Nature Materials*, 2004, **3**, 579-581.
- 538 11. R. Brummer, *Rheology Essentials of Cosmetic and Food Emulsions*, Springer Berlin Heidelberg,
539 2006.
- 540 12. N. A. Peppas, *Hydrogels in Medicine and Pharmacy: Fundamentals*, CRC Press, 2019.
- 541 13. Y. C. Fung, *Biomechanics: Mechanical Properties of Living Tissues*, Springer New York, 2013.
- 542 14. T. G. Mason, *Current Opinion in Colloid & Interface Science*, 1999, **4**, 231-238.
- 543 15. P. J. Lu and D. A. Weitz, *Annual Review of Condensed Matter Physics*, 2013, **4**, 217-233.
- 544 16. D. Vlassopoulos and M. Cloitre, *Current Opinion in Colloid & Interface Science*, 2014, **19**, 561-
545 574.
- 546 17. Z. Adamczyk and P. Warszynski, *Adv. Colloid Interface Sci.*, 1996, **63**, 41-149.
- 547 18. J. N. Wilking, T. E. Angelini, A. Seminara, M. P. Brenner and D. A. Weitz, *MRS Bulletin*, 2011, **36**,
548 385-391.
- 549 19. A. D. Benjamin, R. Abbasi, M. Owens, R. J. Olsen, D. J. Walsh, T. B. LeFevre and J. N. Wilking,
550 *Biomedical Physics & Engineering Express*, 2019, **5**, 1-10.
- 551 20. R. G. Larson, *The Structure and Rheology of Complex Fluids*, OUP USA, 1999.
- 552 21. T. G. Mason and D. A. Weitz, *Physical Review Letters*, 1995, **75**, 2770-2773.
- 553 22. G. Lee, S.-B. Han, J.-H. Lee, H.-W. Kim and D.-H. Kim, *ACS Biomaterials Science & Engineering*,
554 2019, **5**, 3735-3752.
- 555 23. S. Verbruggen, *Mechanobiology in Health and Disease*, Elsevier Science, 2018.
- 556 24. J. C. Erhart-Hledik, E. F. Chehab, J. L. Asay, J. Favre, C. R. Chu and T. P. Andriacchi, *Osteoarthritis
557 and cartilage*, 2021, DOI: 10.1016/j.joca.2021.02.006.
- 558 25. D. L. Zignego, J. K. Hilmer and R. K. June, *Journal of biomechanics*, 2015, **48**, 4253-4261.
- 559 26. T. G. Mason, J. Bibette and D. A. Weitz, *Physical Review Letters*, 1995, **75**, 2051-2054.
- 560 27. P. Menuet, S. Seiffert, J. Sprakel and D. A. Weitz, *Soft Matter*, 2012, **8**, 156-164.
- 561 28. F. L. Leite, C. C. Bueno, A. L. Da Roz, E. C. Ziemath and O. N. Oliveira, *International Journal of
562 Molecular Sciences*, 2012, **13**, 12773-12856.
- 563 29. M. A. Meyers, P. Y. Chen, A. Y. M. Lin and Y. Seki, *Prog. Mater. Sci.*, 2008, **53**, 1-206.
- 564 30. Y. Liang, N. Hilal, P. Langston and V. Starov, *Adv. Colloid Interface Sci.*, 2007, **134-135**, 151-166.
- 565 31. G. Trefalt, T. Palberg and M. Borkovec, *Current Opinion in Colloid & Interface Science*, 2017, **27**,
566 9-17.
- 567 32. C. Gosse and V. Croquette, *Biophysical Journal*, 2002, **82**, 3314-3329.
- 568 33. L. Wilson, P. T. Matsudaira and M. P. Sheetz, *Laser Tweezers in Cell Biology*, Elsevier Science,
569 1997.
- 570 34. D. G. Grier, *Current Opinion in Colloid & Interface Science*, 1997, **2**, 264-270.
- 571 35. K. Kegler, M. Salomo and F. Kremer, *Physical Review Letters*, 2007, **98**, 058304.
- 572 36. H. J. Butt, R. Berger, E. Bonaccorso, Y. Chen and J. Wang, *Adv. Colloid Interface Sci.*, 2007, **133**,
573 91-104.
- 574 37. H. J. Butt, B. Cappella and M. Kappl, *Surface Science Reports*, 2005, **59**, 1-152.
- 575 38. M. M. van Oene, L. E. Dickinson, B. Cross, F. Pedaci, J. Lipfert and N. H. Dekker, *Sci Rep*, 2017, **7**,
576 1-11.
- 577 39. K. Halvorsen and W. P. Wong, *Biophysical Journal*, 2010, **98**, L53-L55.
- 578 40. T. Hoang, D. S. Patel and K. Halvorsen, *Rev. Sci. Instrum.*, 2016, **87**, 1-5.
- 579 41. D. Yang, A. Ward, K. Halvorsen and W. P. Wong, *Nature Communications*, 2016, **7**, 1-7.
- 580 42. L. Kou, L. Jin, H. Lei, C. Hu, H. Li and X. Hu, *J. Microsc.*, 2019, **273**, 178-188.

- 581 43. J. A. Punnoose, A. Hayden, L. F. Zhou and K. Halvorsen, *Biophysical Journal*, 2020, **119**, 2231-
582 2239.
- 583 44. M. W. H. Kirkness and N. R. Forde, *Biophysical Journal*, 2018, **114**, 570-576.
- 584 45. R. Parthasarathy, *Nature Methods*, 2012, **9**, 724-726.
- 585 46. S. H. Behrens and D. G. Grier, *Journal of Chemical Physics*, 2001, **115**, 6716-6721.
- 586 47. J. Gregory, *Journal of Colloid and Interface Science*, 1974, **51**, 44-51.
- 587 48. M. Elimelech, J. Gregory, X. Jia and R. Williams, *Butterworth-Heinemann Ltd*, 1995.
- 588 49. R. Folkersma, A. J. G. van Diemen and H. N. Stein, *Langmuir*, 1998, **14**, 5973-5976.
- 589 50. K. M. Ohsawa, M.; and Ohshima, H., *Colloid & Polymer Science*, 1986, **264**, 1005-1009.
- 590 51. A. Garg, C. A. Cartier, K. J. M. Bishop and D. Velegol, *Langmuir*, 2016, **32**, 11837-11844.
- 591 52. Z. Adamczyk, A. Bratek-Skicki, P. Dabrowska and M. Nattich-Rak, *Langmuir*, 2012, **28**, 474-485.
- 592 53. E. C. Y. Yan, Y. Liu and K. B. Eisenthal, *Journal of Physical Chemistry B*, 1998, **102**, 6331-6336.
- 593 54. O. El-Gholabzouri, M. A. Cabrerizo and R. Hidalgo-Alvarez, *Journal of Colloid and Interface
594 Science*, 1999, **214**, 243-250.
- 595 55. Y. Tabata and Y. Ikada, *Biomaterials*, 1988, **9**, 356-362.
- 596 56. W. M. Brouwer and R. L. J. Zsom, *Colloids and Surfaces*, 1987, **24**, 195-208.
- 597 57. Y. Luthi, J. Ricka and M. Borkovec, *Journal of Colloid and Interface Science*, 1998, **206**, 314-321.
- 598 58. A. M. Schrader, J. I. Monroe, R. Sheil, H. A. Dobbs, T. J. Keller, Y. X. Li, S. Jain, M. S. Shell, J. N.
599 Israelachvili and S. G. Han, *PNAS*, 2018, **115**, 2890-2895.
- 600 59. J. J. Cras, C. A. Rowe-Taitt, D. A. Nivens and F. S. Ligler, *Biosensors & Bioelectronics*, 1999, **14**,
601 683-688.
- 602 60. P. Warszynski and Z. Adamczyk, *Journal of Colloid and Interface Science*, 1996, **1878**, 283-295.
- 603 61. R. M. Pashley, P. M. McGuiggan, B. W. Ninham and D. F. Evans, *Science*, 1985, **229**, 1088-1089.
- 604 62. Y. I. Rabinovich, J. J. Adler, A. Ata, R. K. Singh and B. M. Moudgil, *Journal of Colloid and Interface
605 Science*, 2000, **232**, 10-16.
- 606 63. Y. I. Rabinovich, J. J. Adler, A. Ata, R. K. Singh and B. M. Moudgil, *Journal of Colloid and Interface
607 Science*, 2000, **232**, 17-24.
- 608 64. K. Cooper, A. Gupta and S. Beaudoin, *Journal of Colloid and Interface Science*, 2000, **228**, 213-
609 219.
- 610 65. K. Cooper, N. Ohler, A. Gupta and S. Beaudoin, *Journal of Colloid and Interface Science*, 2000,
611 **222**, 63-74.
- 612 66. L. Wu, H. Feng, D. M. Guo and B. Zheng, *RSC Advances*, 2014, **4**, 60002-60006.

613

614

615

616

617

618

619

620

621

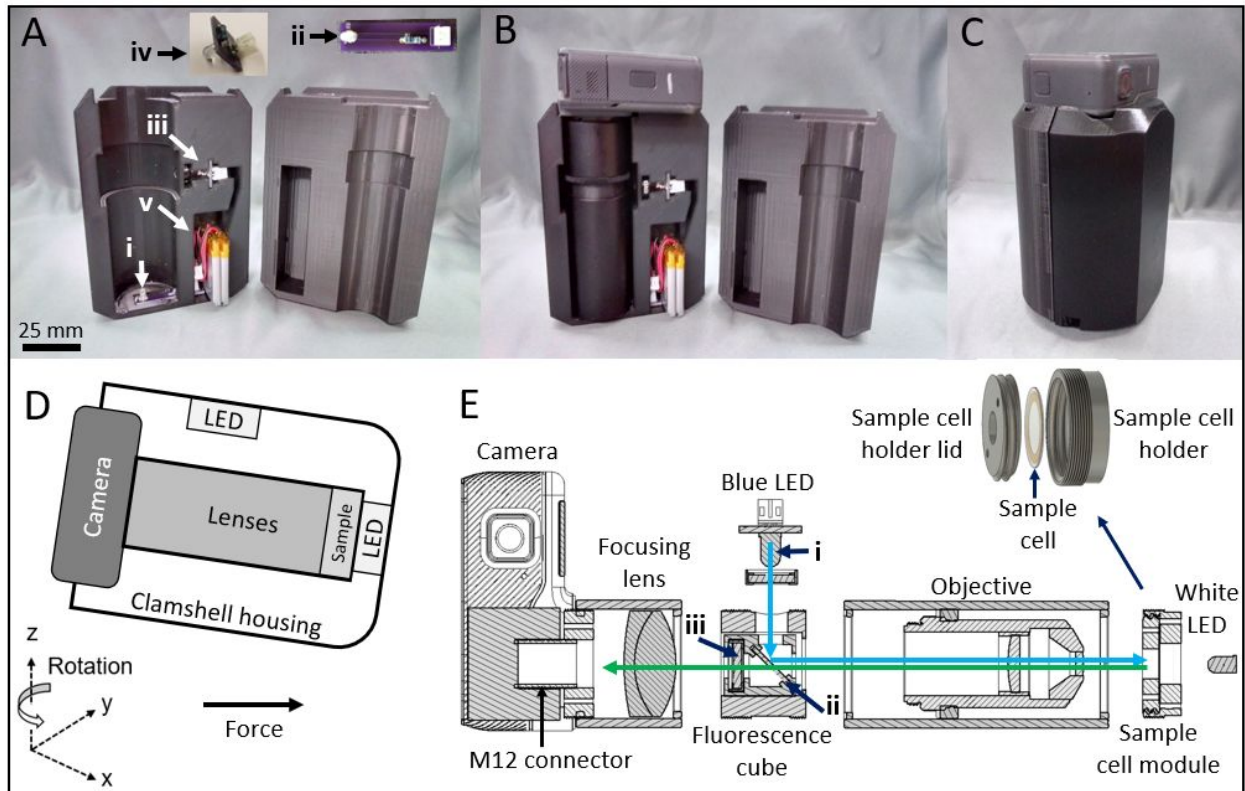
622

623

624

625
626
627
628
629
630

Figure 1



631

632 **Figure 1: Fluorescence CFM construction and assembly.** (A) Two-part clamshell housing for F-CFM module.
633 Brightfield LED (i and ii), fluorescence LED (iii and iv), and lithium polymer (LiPo) battery (v) are built into
634 the housing. Inset: custom printed circuit board for brightfield operation. (B) The F-CFM module fits inside
635 the clamshell housing during assembly. (C) Clamshell housing closes around F-CFM module. Assembly is
636 ready to be lowered into centrifuge bucket. Two camera microphones are visible as small holes to the
637 right and left of the power button (square with red circle). (D) Orientation of the F-CFM components, axis
638 of rotation, and centrifugal force vector during operation. (E) Optical components of the F-CFM module.
639 Fluorescence excitation light (blue) travels from the blue LED and through the excitation filter (i) before
640 reflecting off the dichroic mirror (ii) and reaching the sample. Fluorescence emission light (green) travels
641 from the sample, through the dichroic mirror, the emission filter (iii), and the focusing lens, and into the
642 camera sensor. Brightfield illumination light (not shown) follows same path as fluorescence emission light.
643 Inset: Sample cell holder components. Sample cell holder lid screws into sample cell holder, clamping
644 sample cell in place.

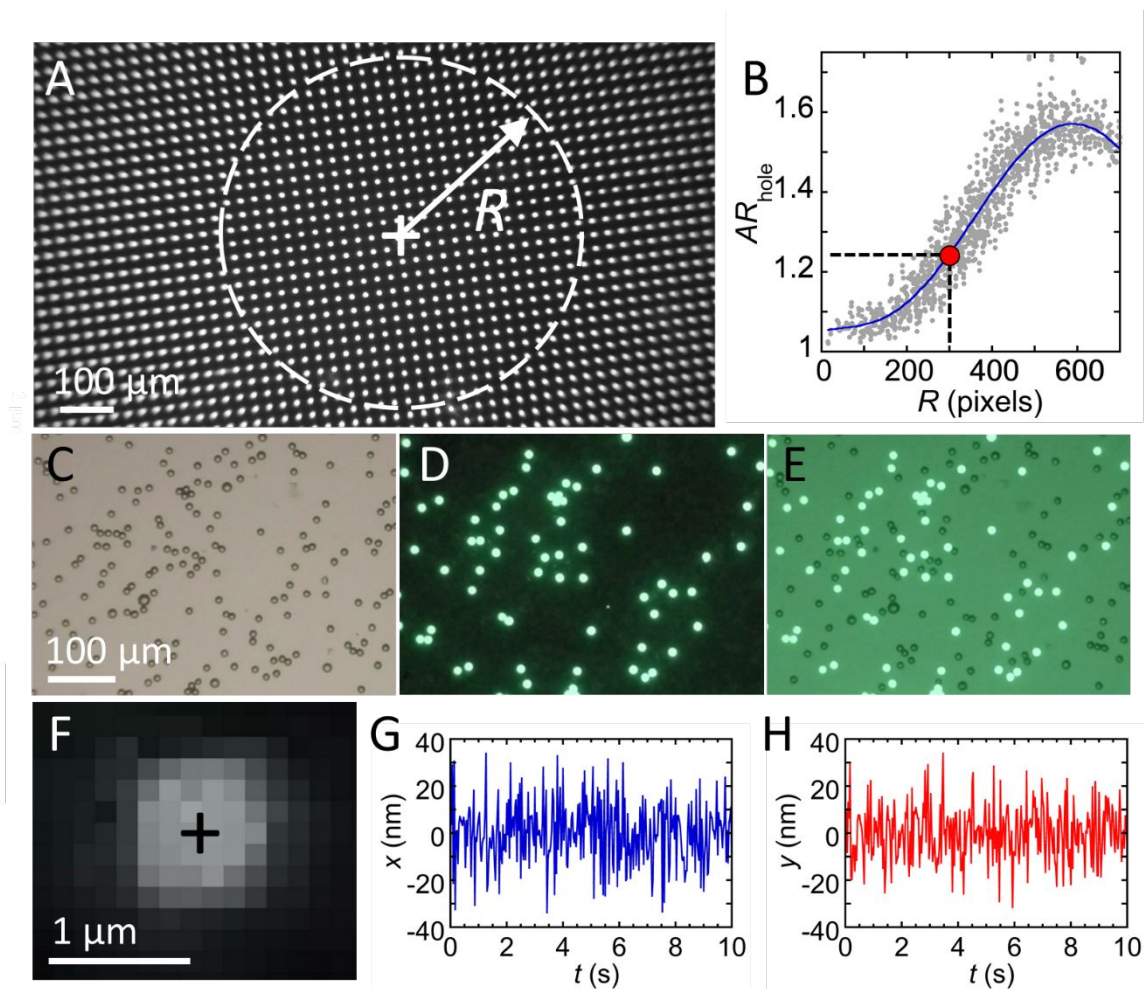
645

646

647

648
649
650
651
652
653
654
655
656
657
658
659
660
661
662
663
664
665
666
667
668
669
670
671
672

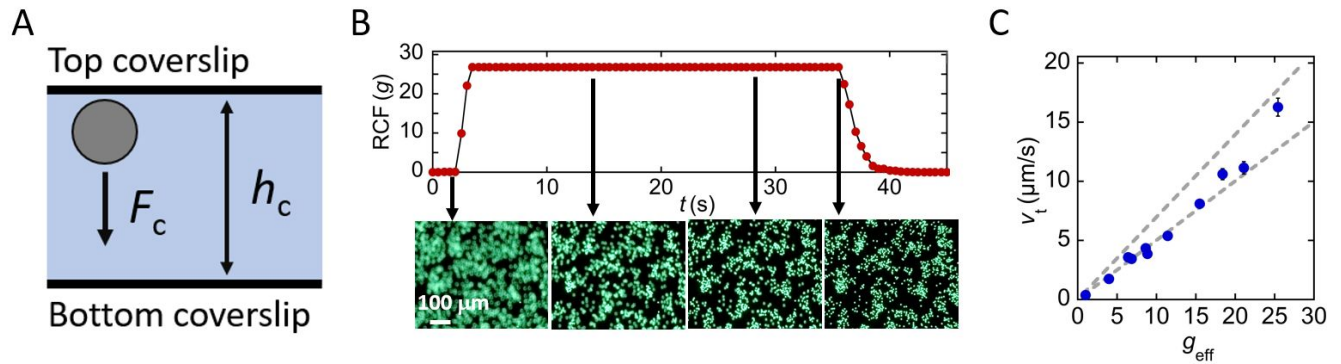
Figure 2

673
674

675 **Figure 2: F-CFM image quality.** (A) Brightfield F-CFM image of photomask grid of uniform circular holes (d
 676 $= 10 \mu\text{m}$) reveals optical aberrations near edges. White cross represents center of focus around which
 677 white dashes define circle of radius R . (B) Plot of apparent hole aspect ratios AR_{hole} as functions of R for
 678 all holes in part A (solid gray circles) fit with a polynomial regression (blue line) to guide the eye (see SI
 679 Table 1 for fitting form). This can be used to quantify a region of defined image quality. For example, white
 680 dashed line in (A) corresponding to $R = 300 \text{ px}$ encloses holes with $AR_{\text{hole}} \leq 1.25$ (red dot). (C-E) F-CFM
 681 images ($350 \times 250 \text{ px}$) of a mixed suspension of green and red fluorescent polystyrene/iron oxide
 682 microspheres ($\bar{d} = 8.3 \mu\text{m}$) captured using (C) brightfield, (D) fluorescence, and (E) concurrent brightfield
 683 and fluorescence imaging modes. Red fluorescent microspheres do not fluoresce under these imaging
 684 conditions. (F) Digitally zoomed grayscale fluorescence F-CFM image of a small microsphere ($\bar{d} = 1.0 \mu\text{m}$)
 685 fixed by drying to the surface of a glass slide. (G and H) Tracking x - and y -positions of sphere from part (F)
 686 over time $t = 10 \text{ s}$ using the radial symmetry method.

687
688
689
690
691
692
693**Figure 3**

694



695

696

697

698

699

700

701

702

703

704

705

706

707

708

709

710

711

712

713

714

715

716

717

718

719

720

721

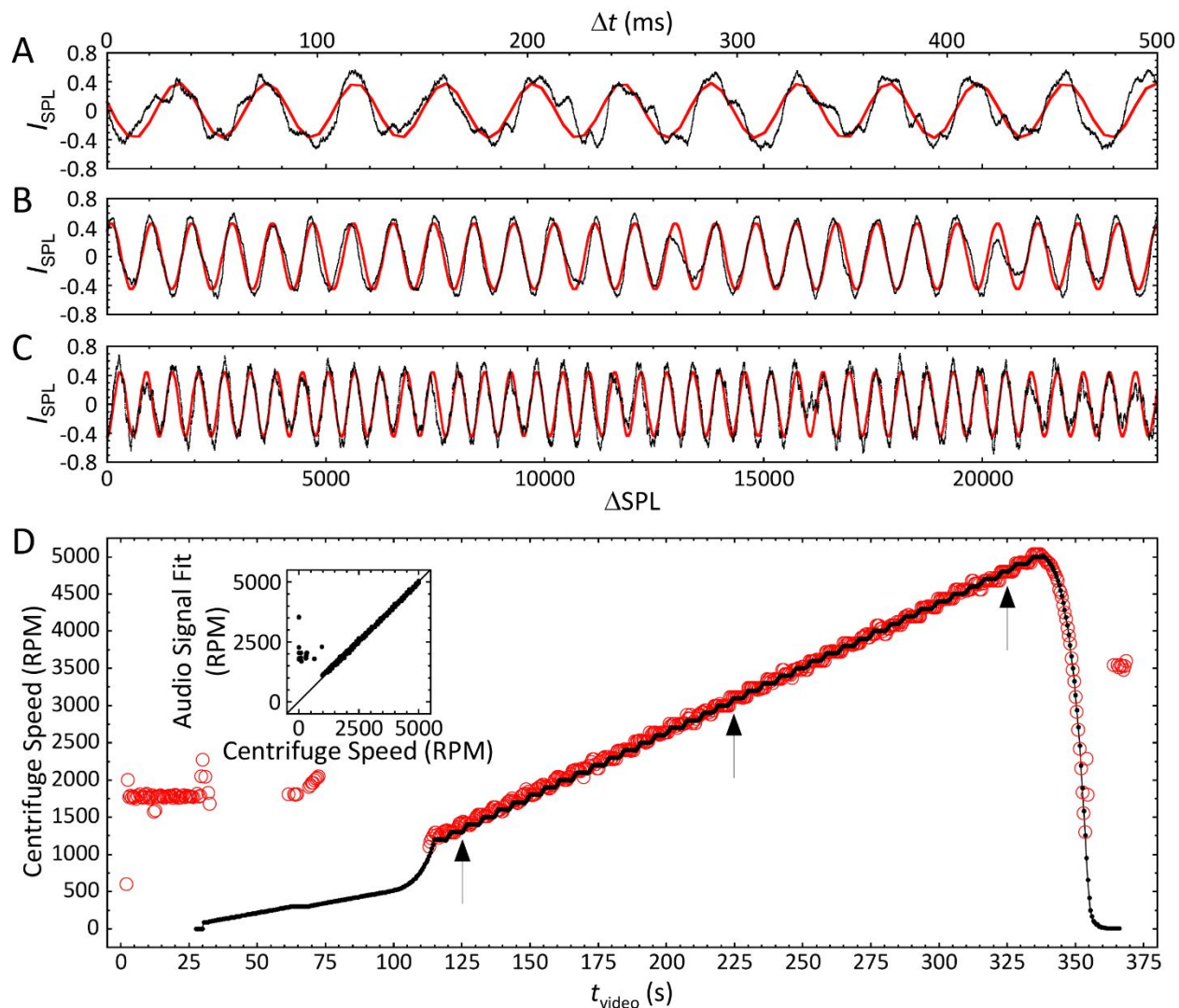
722

723

724

Figure 3: CFM force validation using colloidal sedimentation. (A) Sample cell cross-section. Gray circle represents microsphere at $t = 0$ near top coverslip. Not to scale. (B) Plot of relative centrifugal force (RCF) as a function of time t (s) for a representative sedimentation measurement. Sedimentation of green polystyrene fluorescent microspheres ($\bar{d} = 4.19 \mu\text{m}$) is shown below in representative frames of an optical microscopy movie. (C) Plot of sedimentation terminal velocity v_t (solid blue circles) as a function of effective gravity g_{eff} . Bounding lines represent expected range.

Figure 4



725
 726 **Figure 4: Audio waveforms indicate centrifuge speed. (A-C)** Sections of 48000 Hz audio samples (black
 727 traces) recorded during the beginning, middle, and end of a linearly accelerating F-CFM run. Audio sample
 728 (SPL) traces as functions of increments of time (Δt , upper x-axis) and sample number (ΔSPL , lower x-axis)
 729 are fit using equation, $I_{SPL} = A\sin(ft + \varphi)$ (solid red lines) where I_{SPL} represents recorded sample
 730 intensity (arbitrary units), A amplitude, f frequency (rad), t time (s), and φ offset. Fit parameter f is used
 731 to calculate centrifuge speed values of (A) 1429, (B) 3114, and (C) 4800 RPM operation. (D) Centrifuge
 732 speed (RPM) reported by instrument (solid black circles, solid black line guides the eye) plotted alongside
 733 audio-calculated RPM (open red circles) fit to intervals of 0.5 s (24000 samples at 48000 Hz). Arrows
 734 indicate locations of parts A-C. Inset: Centrifuge speed values (RPM) from both audio signal fits and
 735 magnetic encoder at corresponding times show excellent agreement when RPM > 1000.

736

737

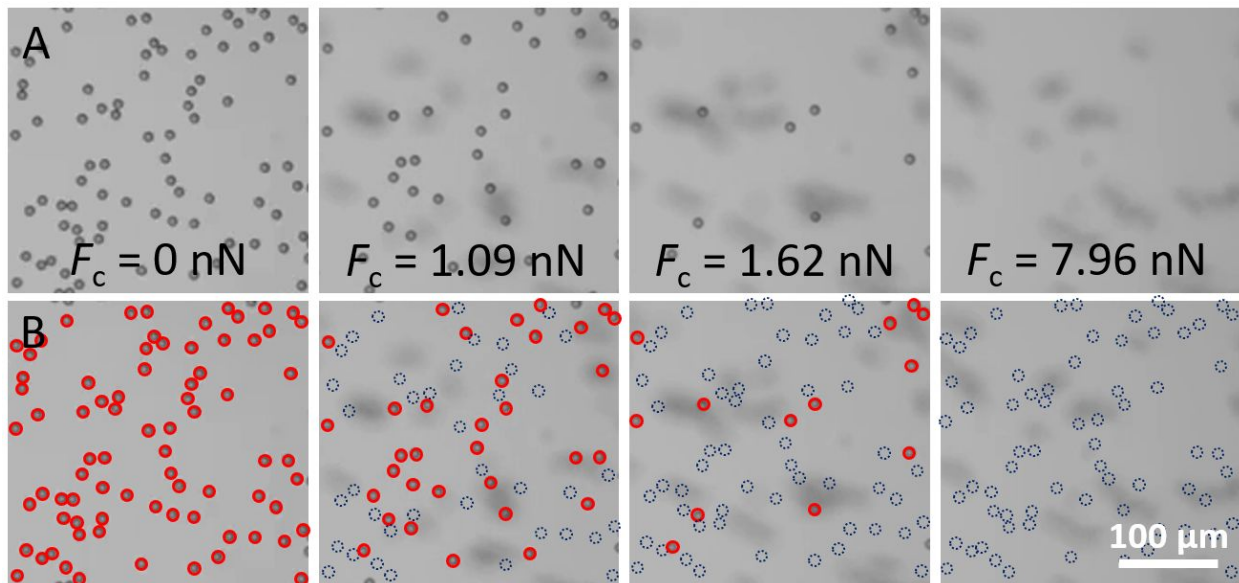
738

739

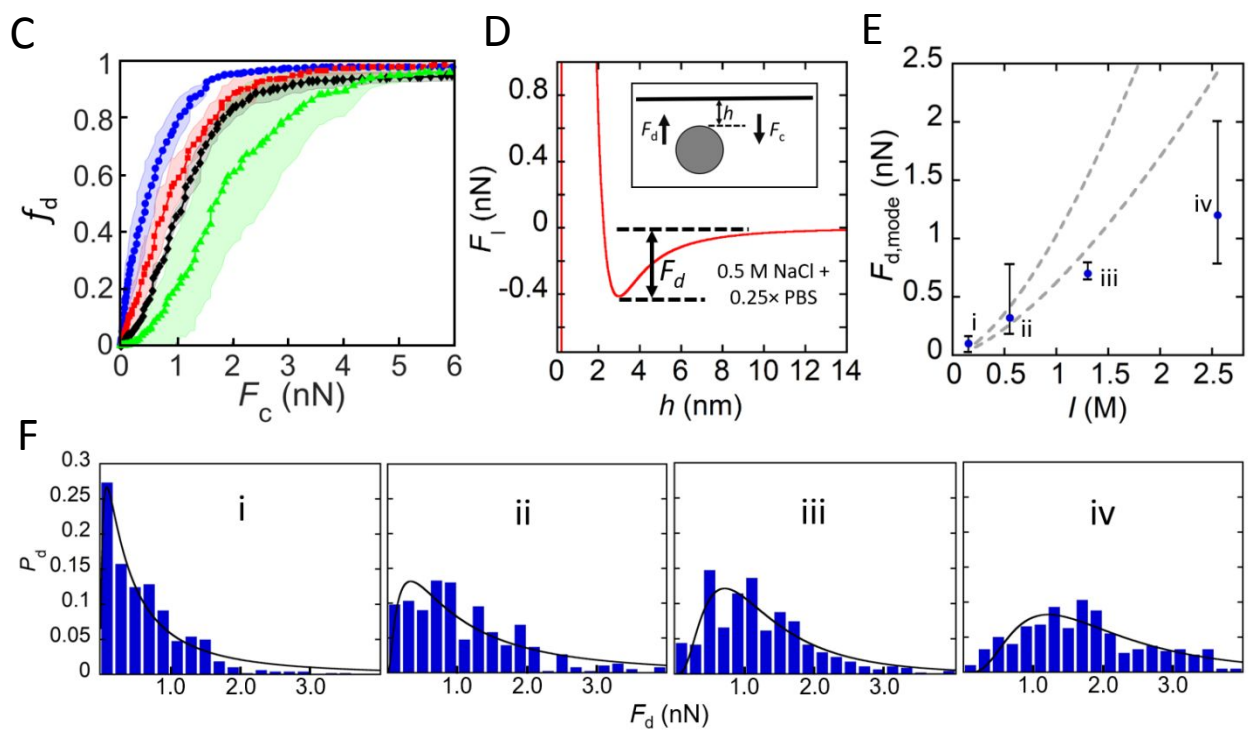
740

741

Figure 5

742
743
744

745

746
747
748
749
750
751

752 **Figure 5:** Colloid detachment force distributions as functions of electrolyte concentrations. (A)
753 Representative optical microscopy images (cropped for better visualization) recorded by the F-CFM show
754 electrostatically-stabilized polystyrene/iron oxide colloidal microspheres ($\bar{d} = 10.4 \mu\text{m}$) being detached

755 from a glass coverslip surface during a force ramp from 1 - 283 relative centrifugal force (RCF). Images are
756 cropped to represent the area of best focus. **(B)** Images from **(A)** indicating attached, in-focus bead
757 locations (solid open red circles) and former locations (dashed open blue circles) of now detached, out-
758 of-focus beads. Scale bar = 100 μm **(A and B)** **(C)** Fractions of total colloids detached f_d as a function of
759 applied centrifugal force F_c for NaCl concentrations 0.1 M (solid blue circles), 0.5 M (solid red squares),
760 1.25 M (solid black diamonds), and 2.5 M (solid green triangles). Solid lines represent the averages of
761 three runs and transparent envelopes indicate one standard deviation. **(D)** Estimated interaction force F_I
762 as function of gap distance h calculated using DLVO theory predicts a detachment force $F_d = 0.040$ nN for
763 0.5 M NaCl + 0.25 \times PBS. Chosen y -axis range does not allow the depth of primary minimum or height of
764 energy barrier to be seen. Inset: Schematic of a bead at distance h from glass slide surface subjected to
765 centrifugal force F_c and detachment force F_d . **(E)** Average detachment force $F_{d,mode}$ (solid blue circles) from
766 the distribution peaks in **(F)** as a function of ionic strength I . Bounding lines represent expected range (see
767 **SI Note 6** for parameter assumptions and **SI Table 3** for upper and lower fit parameters). **(F)** Normalized
768 probability distributions of detachment forces for each experimental condition (i) 0.1 M, (ii) 0.5 M, (iii)
769 1.25 M, and (iv) 2.5 M, each with 0.25 \times PBS. Solid lines represent fits to log-normal distribution function
770 **(SI Table 2)**.
771